

Low-Coordinated Co-N-C on Oxygenated Graphene for Efficient Electrocatalytic H₂O₂ Production

Haisheng Gong, Zengxi Wei, Zhichao Gong, Jingjing Liu, Gonglan Ye, Minmin Yan, Juncai Dong, Christopher Allen, Jianbin Liu, Kang Huang, Rui Liu, Guanchao He, Shuangliang Zhao,* Huilong Fei**

H. Gong, Z. Gong, J. Liu, Prof. G. Ye, M. Yan, J. Liu, K. Huang, R. Liu, G. He, Prof. H. Fei
Advanced Catalytic Engineering Research Center of the Ministry of Education, State Key
Laboratory for Chemo/Biosensing and Chemometrics, and College of Chemistry and
Chemical Engineering, Hunan University, Changsha 410082, China

E-mail: glye@hnu.edu.cn, hlfei@hnu.edu.cn.

Dr. Z. Wei, Prof. S. Zhao

Guangxi Key Laboratory of Petrochemical Resource Processing and Process Intensification
Technology and School of Chemistry and Chemical Engineering, Guangxi University,
Nanning, 530004, China

E-mail: szhao@gxu.edu.cn

Dr. J. Dong

Beijing Synchrotron Radiation Facility, Institute of High Energy Physics, Chinese Academy
of Sciences, Beijing 100049, P. R. China

Dr. C. Allen

Department of Materials, University of Oxford, Parks Road, Oxford, OX1 3PH, UK and
electron Physical Science Imaging Centre, Diamond Lightsource Ltd., OX11 0DE, UK.

Keywords: electrochemical H₂O₂ production, single-atom catalyst, electronic structure, low
coordination, epoxide groups, microwave synthesis

Abstract: Electrochemical H₂O₂ production through the 2-electron oxygen reduction reaction (ORR) is a promising alternative to energy-intensive anthraquinone process. Herein, by simultaneously regulating the coordination number of the atomically dispersed cobalt sites and the nearby oxygen functional groups *via* a one-step microwave thermal shock, we obtain a highly selective and active Co-N-C electrocatalyst for H₂O₂ electrosynthesis that exhibits a high H₂O₂ selectivity (91.3%), outstanding mass activity (44.4 A g⁻¹ at 0.65 V) and large kinetic current density (11.3 mA cm⁻² at 0.65 V) in 0.1 M KOH. In strong contrast to the typical Co-N₄ moieties for the 4-electron ORR, the present Co-N-C catalyst possesses a low-coordinated Co-N₂ configuration and abundant epoxide groups, which work in synergy for promoting the 2-electron ORR, as demonstrated by a series of control experiments and theoretical simulations. This work may provide an effective avenue to modulating the composition and structure of electrocatalysts at the atomic scale, leading to the development of new electrocatalysts with unprecedented reactivity.

1. Introduction

The ever-growing demand of hydrogen peroxide (H₂O₂) in daily life and various industrial processes has driven it as one of the 100 most important global chemicals.^[1] It is predicted that the market need for H₂O₂ would reach about 6 million tons in 2024.^[2] Currently, the industrial production of H₂O₂ is predominantly achieved by an energy- and waste-intensive anthraquinone process that needs complex infrastructures, tedious extraction and additional discreet transportation.^[3] Therefore, it is imperative to develop a more ecofriendly and sustainable alternative technology for H₂O₂ production. Selective electrocatalytic oxygen reduction reaction (ORR) *via* the 2-electron pathway appears to be an attractive and feasible route that enables portable, on-demand and distributed H₂O₂ synthesis.^[4] However, the production of H₂O₂ through ORR competes with the 4-electron ORR pathway towards H₂O and consequently requires highly active and selective electrocatalysts. The selectivity of the ORR electrocatalysts

is strongly correlated with the electronic structure that governs the absorption strength of the reaction intermediates on the active sites. Specifically, for the selective production of H_2O_2 , the catalysts need to absorb the reaction intermediate OOH^* with an optimal binding energy that could facilitate its reduction to H_2O_2 with the preservation of the O–O bond, but suppress it from being further reduced or dissociated to O^* and OH^* that will lead to the formation of H_2O .^[5-7] Platinum-group metals (PGMs) are known as the state-of-the-art 4-electron ORR catalysts, but researchers found that PGMs can also selectively catalyze the 2-electron ORR by forming alloys with catalytically inert mercury (*e.g.*, Pt-Hg and Pd-Hg), which can isolate the active sites of PGMs and thus prevent the breaking of O–O bond during ORR.^[8-11] Nevertheless, the scarceness and low mass activity of PGMs become a great obstacle for their practical use, calling for alternative electrocatalysts.

Metal- and nitrogen-doped carbons (M-N-Cs) as a unique class of single atom catalysts (SACs) have attracted considerable interests in electrocatalysis.^[12] The electronic structure of M-N-Cs can be fine-tuned by a variety of knobs such as the central metals, the coordination environment or the composition of the surrounding carbon matrix, leading to optimized catalytic performance in different electrochemical energy conversion processes, including ORR, CO_2 reduction, H_2/O_2 evolution reaction, N_2 reduction reaction, *etc.*^[12-14] Particularly, M-N-Cs (M=Co) have recently been intensively studied as 2-electron ORR catalysts and the regulation of the electronic structure plays critical roles in determining their performance.^[15] The Co centers in Co-N-C catalysts typically adopt the thermodynamically stable Co-N₄ porphyrin-like moiety that is more favorable for the 4-electron ORR.^[16-20] Interestingly, recent studies suggested that modulating the oxygen functional groups near the Co-N₄ site could effectively tune its electronic structure and therefore steer the ORR process for H_2O_2 production.^[18-19, 21-22] For example, Li *et al.* used concentrated nitric acid to oxidize the Co-N-C catalyst and the as-treated catalyst exhibited a significant increase in oxygen content that led to enhanced

1 selectivity towards H_2O_2 .^[22] Zhang *et al.* treated the Co-N-C catalyst with electrochemical
2 oxidation and H_2O_2 -involved chemical oxidation, which introduced abundant epoxy groups that
3 resulted in enhanced performance for H_2O_2 synthesis.^[19] However, the harsh oxidation
4 conditions applied in these pioneering studies not only complicate the preparation process of
5 oxygen-rich Co-N-C catalysts, but also may lead to the demetallation and stability issues of the
6 atomic metal sites.^[23] Other than the oxygen functional groups introduced on the carbon support,
7 the coordination number of the atomic metal sites is another key factor in determining the
8 electronic structure of M-N-Cs.^[24] In this regard, vast studies have found that low-coordinated
9 M-N_x ($x < 4$) moieties can present better catalytic performance for CO_2 reduction than the M-
10 N_4 moieties.^[25-29] However, the effect of lowering the coordination number of M-N-Cs on the
11 2-electron ORR selectivity towards H_2O_2 remains seldomly studied, which could be partially
12 ascribed to the limited synthetic approach to the low-coordinated M-N_x sites that are less stable
13 than the M-N₄ counterparts.^[24, 26, 29]

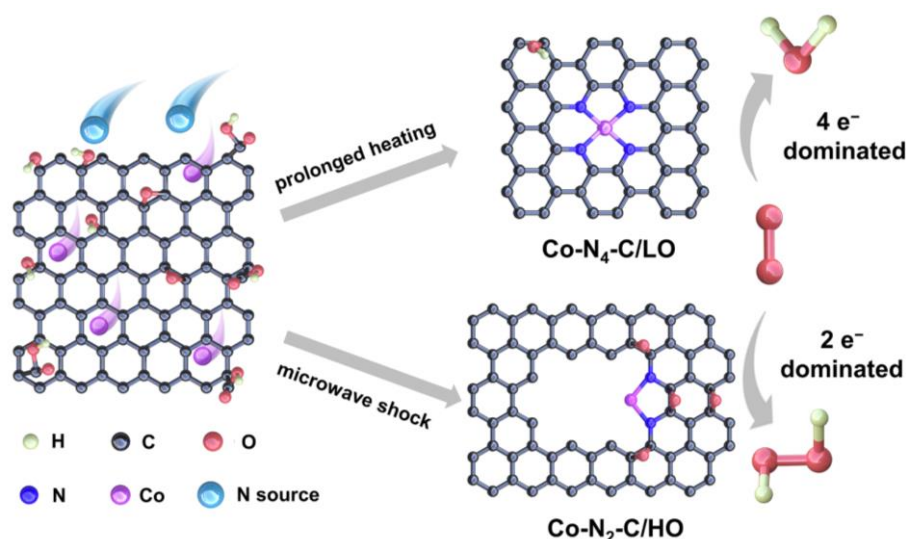
14 Ultrashort thermal shock (*e.g.*, Joule heating,^[30-31] solid-state microwave irradiation^[32-34])
15 with rapid heating and quenching capability has recently been utilized to synthesize kinetically-
16 controlled materials with unprecedented composition, structure and reactivity that are
17 inaccessible by conventional prolonged high-temperature processing.^[35] For example, Hu *et al.*
18 synthesized a wide range of high-entropy multimetallic nanoparticles by rapid electrical Joule
19 heating.^[36-37] Tour *et al.* applied a similar strategy to obtain graphene with turbostratic
20 arrangement between the stacked layers,^[30] and metastable 1T-phase MoS_2 and WS_2 .^[38] Further,
21 thermal shocking, with the benefits of minimizing the high-temperature atom aggregation, has
22 recently been employed to synthesize atomically dispersed metal catalysts.^[31-32] However, these
23 studies focused on the demonstration of new synthetic approach to SACs, while little attention
24 was paid to the effects of the synthetic methods on the coordination configuration, electronic
25 structure and catalytic reactivity of the resulted SACs.

Herein, by making use of a facile and transient microwave irradiation treatment, we simultaneously achieved the regulation of the coordination number and the surrounding oxygenated functional groups in Co-N-C SACs. The as-prepared catalyst possesses a low-coordinated Co-N₂ configuration and high content of C-O-C epoxide groups (denoted as Co-N₂-C/HO thereafter). In comparison to the typical Co-N₄-C/LO with low content of epoxide groups by conventional prolonged annealing method, Co-N₂-C/HO shows a significantly enhanced performance for H₂O₂ production with a high selectivity (91.3%), prominent mass activity (44.4 A g⁻¹ at 0.65 V) and large kinetic current density (11.3 mA cm⁻² at 0.65 V), making it one of the most active SACs for H₂O₂ electrosynthesis. Control experiments and theoretical calculations suggest that the high activity and selectivity of Co-N₂-C/HO come from its unique electronic structure resulted from the synergy of the low coordination configuration and oxygen functional groups.

2. Results and Discussion

To synthesize Co-N₂-C/HO, a solid mixture of amine-functionalized graphene oxide and small amounts of Co precursor was treated with a 1-s-long microwave pulse (**Scheme 1**, details were provided in Experimental Section). A similar microwave-assisted synthesis has been previously reported by us to access a variety of graphene-supported SACs,^[32] while the present study focuses on the effects of the instant heating and quenching procedure on the composition, structure and catalytic reactivity of the resulted SACs. It is proposed that the instant microwave irradiation could generate kinetically-controlled Co-N_x moieties. For comparison, a thermodynamically stable Co-N₄-C/LO catalyst was synthesized by annealing the mixture of graphene oxide and Co precursor in NH₃ atmosphere at high temperature for 1-h-long period. As shown in the X-ray diffraction (XRD) patterns (Figure S1), Co-N₂-C/HO and Co-N₄-C/LO exhibit two diffraction peaks belonging to the (002) and (100) planes of graphitized carbon without Co-derived peaks, indicating the absence of metal atom aggregation. The Raman

spectrum of Co-N₂-C/HO presents a lower D-to-G band ratio and a more distinct 2D band compared to Co-N₄-C/LO (Figure S2), manifesting the more efficient reduction and exfoliation of graphene oxides by the microwave heating.^[2, 32]



Scheme 1. Schematic diagram of the synthesis route to Co-N₄-C/LO and Co-N₂-C/HO.

To explore the chemical states and elemental composition of the samples, X-ray photoelectron spectroscopy (XPS) survey spectra reveal the coexistence of C, N and O peaks and the absence of Co peaks in both samples due to their low contents (**Figure 1a**). The Co contents in Co-N₂-C/HO and Co-N₄-C/LO were estimated to be 0.88 wt% and 0.10 wt%, respectively, by inductively coupled plasma mass spectrometry (ICP-MS) (Table S1). From the N 1s XPS spectra (Figure S3), Co-N₂-C/HO is enriched with graphitic N and deficient with pyridinic N, in contrast to Co-N₄-C/LO, possibly due to the transformation of the pyridinic N to more stable graphitic N under the microwave-induced high-energy environment.^[32, 39] Similar features of N species in Co-N₂-C/HO and Co-N₄-C/LO were observed in N K-edge near-edge X-ray absorption fine structure (NEXAFS) spectra (Figure S4a). Figure 1a further reveals that Co-N₂-C/HO has an obviously higher oxygen content (7.9 at%) than that of Co-N₄-C/LO (5.70 at%), which can be ascribed to the much shorter exposure duration to high-temperature environment during the synthesis of Co-N₂-C/HO. The higher content of oxygen

in Co-N₂-C/HO was confirmed by combustion elemental analysis (Table S2). The high-resolution O 1s XPS spectra can be deconvoluted into three oxygen functional groups (C=O, C-O-C epoxides and C-OH) (Figure 1b, c).^[18] It can be observed that Co-N₂-C/HO shows a much stronger C-O-C peak (3.80 at%) than Co-N₄-C/LO (1.68 at%). The high-resolution C 1s spectra in Figure 1d involve three carbon species (C=C, C-O-C/C-N, C=O), and a higher C-O-C/C-N peak was observed in Co-N₂-C/HO (19.9%) than Co-N₄-C/LO (16.8%), consistent with the results from O 1s XPS spectra. The difference of oxygen functional groups over Co-N₂-C/HO and Co-N₄-C/LO was confirmed in Fourier-transform infrared spectroscopy (FTIR) (Figure 1e), where a stronger peak at about 1200 cm⁻¹ assigned to C-O-C epoxide was observed in Co-N₂-C/HO compared to Co-N₄-C/LO.^[2, 18] The O K-edge NEXAFS spectrum of Co-N₂-C/HO exhibits a more intense peak at 540.5 eV that can be ascribed to the transitions of the O 1s core level to π^* states and σ^* states from C-O bonds (*e.g.*, C-O-C epoxides) (Figure S4b),^[2, 18] further revealing the enrichment of oxygen-containing functional groups in Co-N₂-C/HO. For the high-resolution Co 2p XPS spectra (Figure 1f), the Co 2p peaks of Co-N₂-C/HO shift slightly to the lower binding energy compared to those of Co-N₄-C/LO, indicating the lower oxidation state of Co in Co-N₂-C/HO.

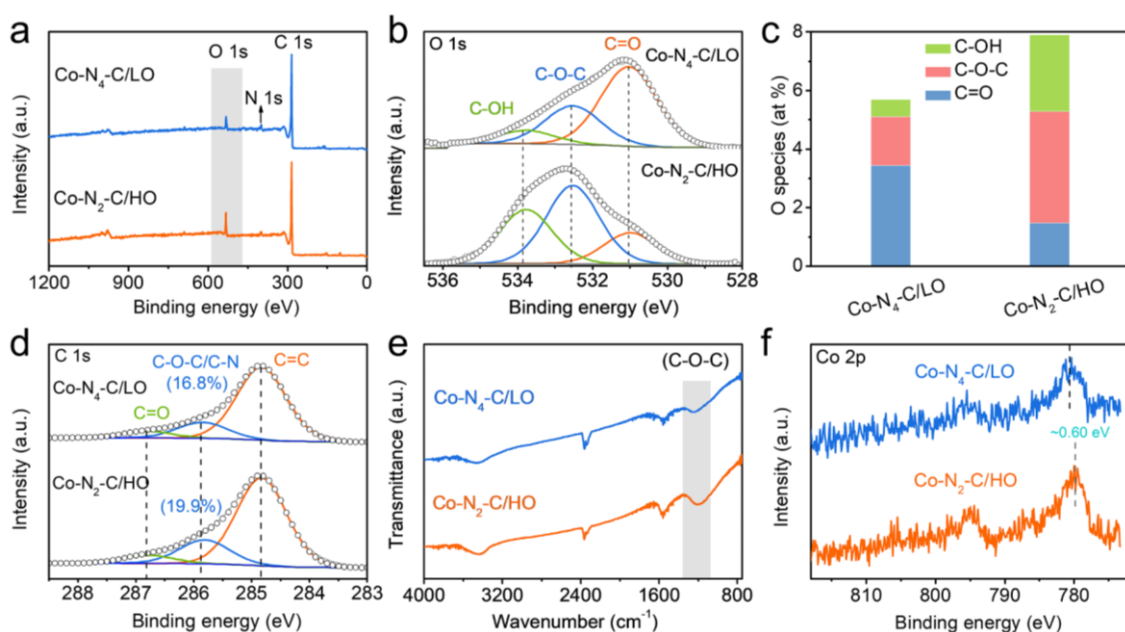
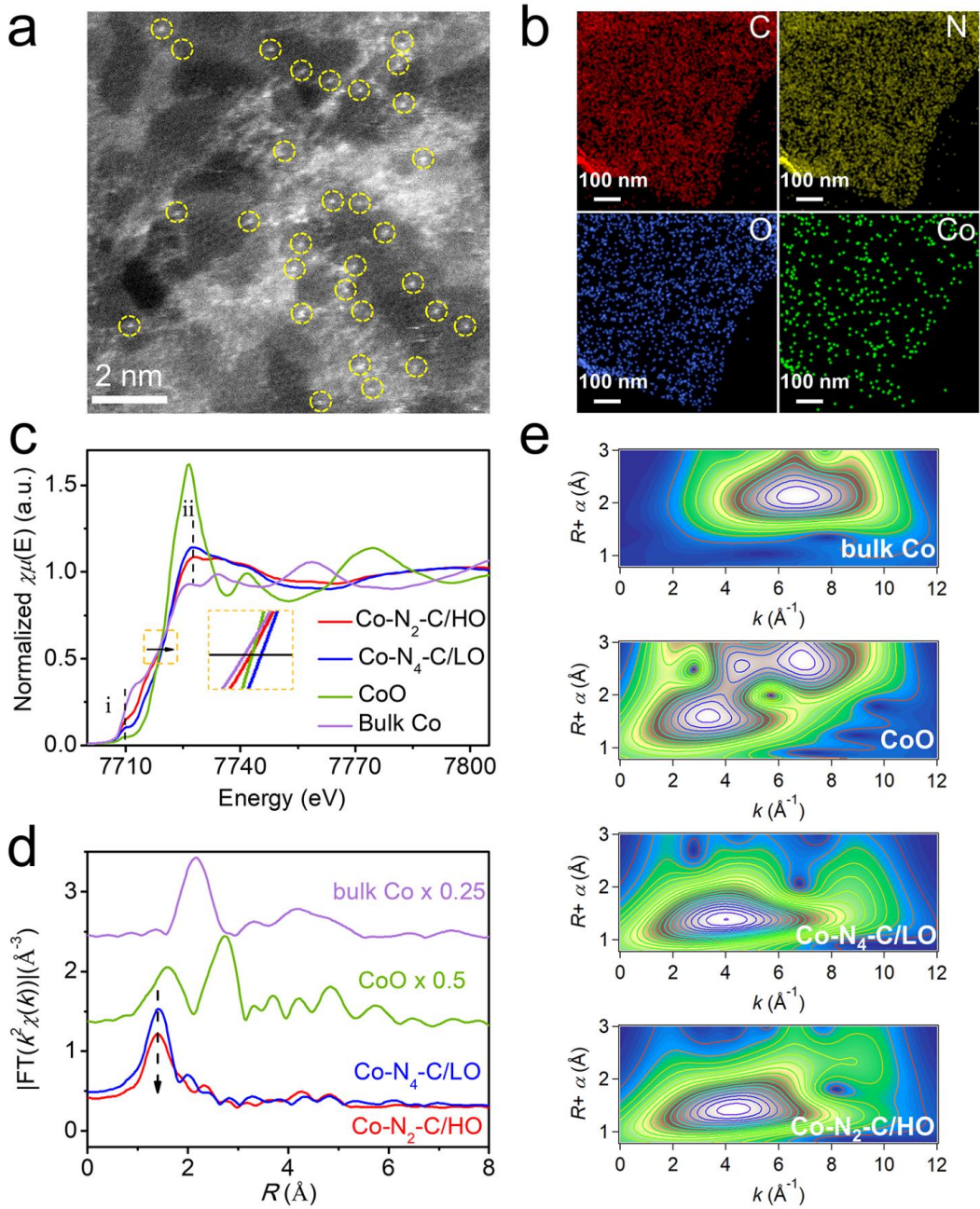


Figure 1. Compositional characterizations. (a) XPS survey spectra of Co-N₄-C/LO and Co-N₂-C/HO. (b) High-resolution O 1s XPS spectra of Co-N₄-C/LO and Co-N₂-C/HO. (c) The atomic percentages of oxygen species in Co-N₄-C/LO and Co-N₂-C/HO. (d) High-resolution C 1s XPS spectra, (e) FTIR spectra, and (f) high-resolution Co 2p XPS spectra of Co-N₄-C/LO and Co-N₂-C/HO.

High-angle annular dark-field scanning transmission electron microscopy (HAADF-STEM) image of Co-N₂-C/HO reveals that the Co metals are atomically dispersed throughout the graphene matrix (**Figure 2a**). Energy dispersive X-ray spectroscopy (EDS) mapping of Co-N₂-C/HO reveals the homogeneous distribution of C, N, O and Co elements (Figure 2b). X-ray absorption spectroscopy was then used to provide structural information on the valence states and coordination environment.^[40] Co K-edge X-ray absorption near-edge structures (XANES) of Co-N₂-C/HO and Co-N₄-C/LO show similar profiles (Figure 2c), suggesting their analogous bonding configurations. Careful examination of the pre-edge at around 7710 eV suggests the evidently increased 1s→3d transition peak i in Co-N₂-C/HO (Figure 2c), signifying rather distorted D_{4h} centrosymmetry of the Co sites.^[32] Compared to Co-N₄-C/LO, an obviously reduced peak ii (1s→4p_{xy} transitions) was observed for Co-N₂-C/HO, revealing a defective graphene architecture and low-coordinated coordination configuration around the Co atoms. Comparing the Co K-edge position at the half of the edge maximum intensity, it can be found that the valence state of Co in Co-N₂-C/HO is lower than that of Co-N₄-C/LO,^[32, 41] which is consistent with Co 2p XPS results. Fourier transform (FT) magnitudes of Co K-edge extend X-ray absorption fine structure (EXAFS) of Co-N₂-C/HO and Co-N₄-C/LO display a dominant peak at ca. 1.4 Å corresponding to the Co-N coordination and no obvious peaks from Co-Co contribution can be observed (Figure 2d). In addition, Co-N₂-C/HO presents an evidently lower peak intensity of Co-N compared to Co-N₄-C/LO, manifesting a lower N coordination number of the Co center, in line with the results from the Co K-edge XANES. The atomic dispersion of

1 the Co was further confirmed by EXAFS wavelet transform (WT) (Figure 2e), where only one
2 intensity maximum at $\approx 4.0 \text{ \AA}^{-1}$ shows up in Co-N₂-C/HO and Co-N₄-C/LO. Quantitative
3 structural results were extracted by least-squares EXAFS curve-fitting analysis (Figure S5 and
4 Table S3), suggesting that the coordination number of Co-N₂-C/HO and Co-N₄-C/LO is 2.0 and
5 3.8, respectively.



6
7 **Figure 2.** Characterizations of atomistic structure. (a) HAADF-STEM image of Co-N₂-C/HO.
8 (b) EDS elemental mapping of Co-N₂-C/HO. (c) Co K-edge XANES spectra of Co-N₂-C/HO,

Co-N₄-C/LO and reference samples (cobalt oxide and bulk cobalt). (d) Fourier transform magnitudes of Co K-edge EXAFS for Co-N₂-C/HO, Co-N₄-C/LO and the reference samples. The reference spectra had been reduced in size. (e) Wavelet transforms for Co-N₂-C/HO, Co-N₄-C/LO and the reference samples.

The ORR performance was evaluated on a rotating ring-disk electrode (RRDE) at 1600 r.p.m. in an O₂-saturated 0.1 M KOH electrolyte. The Pt ring electrode was held at 1.2 V to quantify the amount of H₂O₂ produced on the disk electrode. The collection efficiency of RRDE was calibrated to be 0.237 (Figure S6). The optimized catalyst loading amount was 37.5 $\mu\text{g cm}^{-2}$ (Figure S7). **Figure 3a** shows the polarization curves for Co-N₂-C/HO, Co-N₄-C/LO and metal-free N-C, with the oxygen reduction current measured on the disk electrode (solid lines) and the H₂O₂ oxidation current on the Pt ring electrode (dashed lines). The corresponding H₂O₂ selectivity as a function of potential was plotted in Figure 3b. Among the three catalysts, Co-N₄-C/LO exhibited the highest oxygen reduction current and most positive onset potential at the disk electrode, indicating its highest ORR activity. However, the corresponding H₂O₂ oxidation current is relatively low and starts at a less positive potential, indicating that Co-N₄-C/LO mainly catalyze the ORR through the 4-electron process. In contrast, Co-N₂-C/HO achieved the highest H₂O₂ production current and selectivity within the entire potential range, along with an onset potential as high as 0.801 V (determined at the current density of 0.15 mA cm^{-2}). Particularly, at 0.7 V, Co-N₂-C/HO exhibited a H₂O₂ production current density of 1.46 mA cm^{-2} and selectivity of 91.3%, which were much higher than those (0.91 mA cm^{-2} and 48.7%) of Co-N₄-C/LO (Figure 3c). The average number of electrons transferred (n) was calculated from the disk current and ring current of RRDE. As shown in Figure S8, Co-N₂-C/HO exhibited an $n = 2.3$, indicating that it mainly catalyzes the ORR through the 2-electron pathway, in contrast to Co-N₄-C/LO with $n = 3.0$. A control sample of LCo-N₂-C/HO with a similar Co content (0.14 wt%) to that of Co-N₄-C/LO (0.10 wt%) was prepared via microwave

irradiation and its selectivity was similar to Co-N₂-C/HO and higher than Co-N₄-C/LO (Figure S9), confirming that the catalytic property is strongly dependent on the heating protocol. In the absence of Co, the control sample of N-C suffered from decreased activity and selectivity for the 2-electron ORR. As a reference sample, the commercial Pt/C catalyst exhibited a diffusion-limited disk current density close to 6 mA cm⁻² with negligible ring current density and H₂O₂ production (Figure S10), suggesting that it catalyzed the ORR via a complete 4-electron process. To correct for mass-transport limitation, the kinetic current density (j_k) for H₂O₂ production was calculated according to the Koutecký–Levich equation. The obtained j_k of Co-N₂-C/HO at 0.65 V is 11.3 mA cm⁻², manifesting its outstanding H₂O₂ production activity that outperforms most of the state-of-the-art catalysts (Figure 3d). Furthermore, the calculated Tafel slope of Co-N₂-C/HO (51.3 mV dec⁻¹) is significantly smaller than those of Co-N₄-C/LO and control samples (Figure S11), signifying its faster reaction kinetics. The mass activity and turnover frequency (TOF) of Co-N₂-C/HO at 0.65 V were estimated to be 44.4 A g⁻¹ and 1.54 s⁻¹, respectively, superior to most of recently reported SACs (Figure 3e, Figure S12 and Table S4). Moreover, Co-N₂-C/HO shows stable activity and selectivity, as demonstrated by the 8-h chronoamperometry test and 2000 cycles of CV test (Figure 3f and Figure S13). The performance of Co-N₂-C/HO was also evaluated in acidic (0.1 M HClO₄) and neutral electrolytes (0.1 M PBS), demonstrating better selectivity towards 2-electron ORR than Co-N₄-C/LO and N-C (Figure S14). To explore the possibility for practical use, Co-N₂-C/HO was casted on a hydrophobic carbon paper and evaluated in an H-cell under a constant current density of 25 mA cm⁻². According to the linear fitting curves between absorbance and titrant (Figure S15), the concentration of H₂O₂ produced can be determined that reached ~1000 mg L⁻¹ within 1 h and ~1800 mg L⁻¹ within 8 h (Figure S16), which can sufficiently satisfy the direct usage in industries including water disinfection and bleaching.^[5, 42]

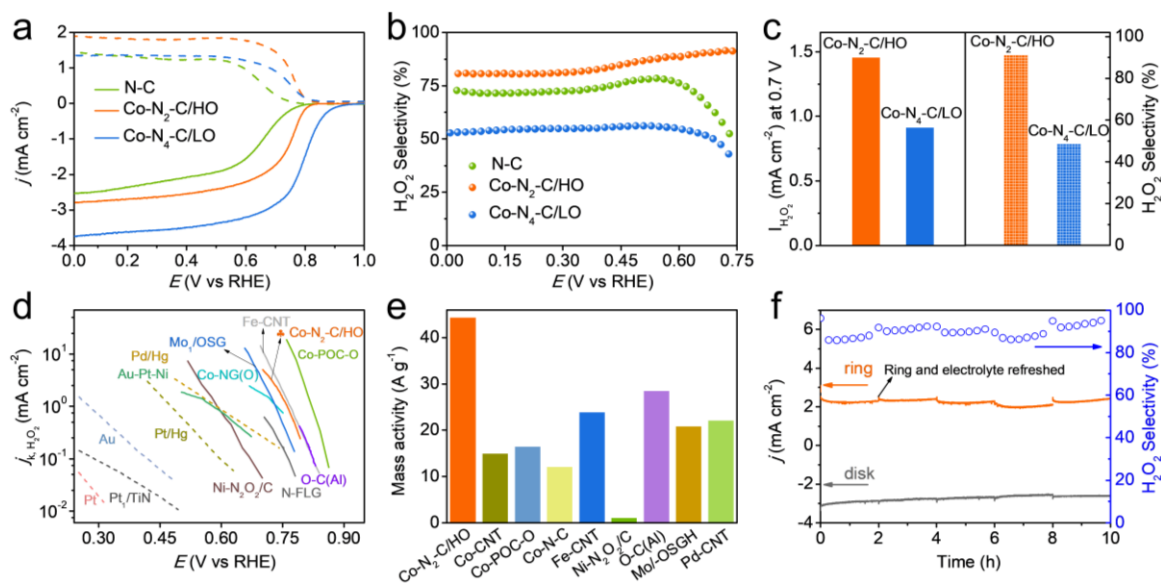


Figure 3. Electrochemical ORR performance. (a) RRDE voltammograms of Co-N₂-C/HO, Co-N₄-C/LO and N-C in an O₂-saturated 0.1M KOH. (b) H₂O₂ selectivity on Co-N₂-C/HO, Co-N₄-C/LO and N-C. (c) Comparison of H₂O₂ current and H₂O₂ selectivity at 0.7 V for Co-N₂-C/HO and Co-N₄-C/LO. (d) Comparison of kinetic current density for H₂O₂ production between Co-N₂-C/HO and catalysts reported in prior works in alkaline media (solid line)^[5, 18, 22, 43-47] and acidic media (dash line).^[9-11, 48-49] (e) Comparison of mass activity at 0.65 V between Co-N₂-C/HO and SACs catalysts reported in literatures under alkaline media.^[5, 22, 44, 46-47, 50] (f) Chronoamperometry stability test of Co-N₂-C/HO at 0.09 V in 0.1 M KOH. The Pt ring electrode was cleaned by cyclic voltammetry scanning from 0 to -0.3 V vs RHE for 40 cycles and the electrolyte was refreshed every 2 h during the chronoamperometry test.

To explore the possible active sites for H₂O₂ production, poisoning study of Co-N₂-C/HO and Co-N₄-C/LO were performed in 0.1 M KOH electrolyte containing 20 mM KSCN. After being immersed in the poisoning electrolyte for 1 h, an apparent decline of disk current density and increased overpotential (η) was observed over Co-N₂-C/HO and Co-N₄-C/LO (Figure S17), confirming the pivotal role of Co center in the activity for H₂O₂ production. To gain insights into the effect of the oxygen functional groups on the H₂O₂ selectivity, Co-N₂-C/HO was treated

under H₂ atmosphere at 500 °C for 1.5 h so as to partially remove the oxygen functional groups. As shown in Figure S18a and S18b, the reduction treatment on Co-N₂-C/HO induced a significant decline in the total oxygen content with a largest decrease of the C-O-C groups. The XRD patterns and Co 2p XPS spectra of reduced Co-N₂-C/HO were similar to those of Co-N₂-C/HO (Figure S18c and S18d), indicating the absence of metal atom aggregation during the H₂ reduction. This is expected as the catalyst had been thermally treated by microwave shocking, the temperature of which could reach > 1000 °C that is much higher than that used for the H₂ reduction (500 °C).^[32, 34] Further, ICP-MS measurements suggested that the Co contents were similar before and after H₂ reduction (Table S1). These results together suggest that the reduction treatment would not lead to the agglomeration of Co atoms and destruction of the Co-N₂ active sites. Comparing the RRDE voltammograms and H₂O₂ selectivity (Figure S19a and S19b), a dramatical decrease of H₂O₂ production current and H₂O₂ selectivity (by 20%) was observed in the reduced Co-N₂-C/HO, manifesting the crucial role of oxygen groups in obtaining the high H₂O₂ selectivity. Another control sample of Co₁-NG(O) with Co-N₄ configuration and rich oxygen functional groups (especially epoxy groups) was synthesized according to the literature.^[18] The catalytic activity and selectivity of this sample was evaluated and compared with other samples. As shown in Figure S20, Co₁-NG(O) presented a lower ORR activity and H₂O₂ selectivity compared to Co-N₂-C/HO, suggesting the crucial role of low coordination configuration in promoting the activity and selectivity for H₂O₂ production. These control experiments demonstrate that the high activity and selectivity of Co-N₂-C/HO come from the synergy of the low coordination configuration and oxygen functional groups. To explore the origin of high H₂O₂ selectivity and the reaction mechanism, hydrogen peroxide reduction reaction was conducted in N₂-saturated 0.1 M KOH electrolyte containing 3.5 mM H₂O₂. As shown in Figure S21, compared to Pt/C and Co-N₄-C/LO, Co-N₂-C/HO shows the lowest H₂O₂ reduction current, suggesting its negligible activity toward the H₂O₂ reduction

1 reaction. This result explained the origin of high H_2O_2 selectivity of Co-N₂-C/HO, which
 2 avoided the further reduction of H_2O_2 product and a $2\text{e}^- + 2\text{e}^-$ mechanism of ORR.^[18, 51-52]

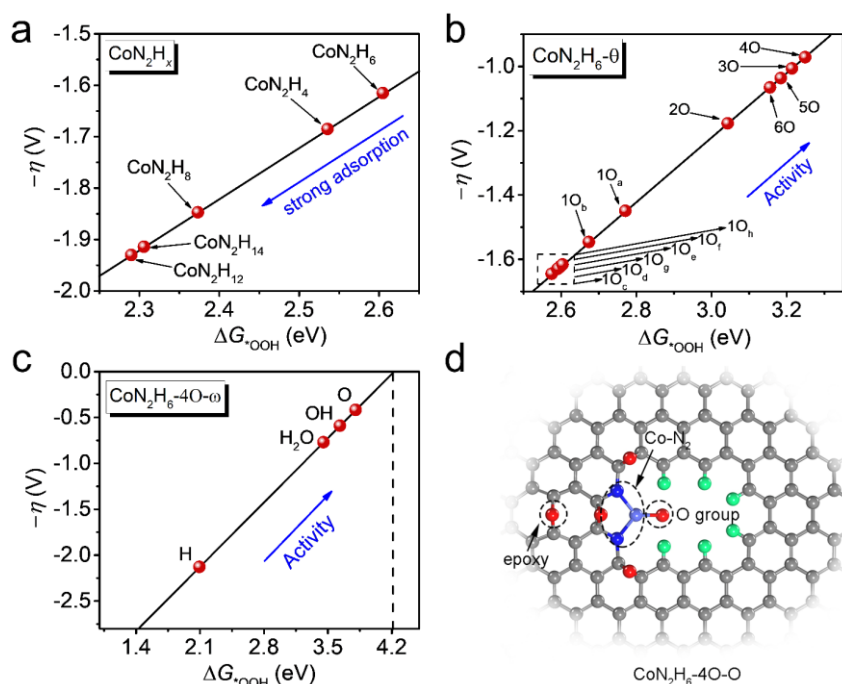


Figure 4. Theoretical studies on the synergy between the Co-N₂ sites and oxygen groups on the carbon matrix. (a) The plot of η as a function of ΔG^*_{OOH} for the CoN₂H_x ($x = 4, 6, 8, 12, 14$) moieties. (b) The plot of η as a function of ΔG^*_{OOH} for CoN₂H₆ with epoxy groups (CoN₂H₆-θ) with different locations and coverages. (c) The introduced solvent species on the Co site of CoN₂H₆ with 4 epoxy groups (CoN₂H₆-4O-ω, ω = H, H₂O, OH or O). The η was plotted as a function of ΔG^*_{OOH} for CoN₂H₆-4O-ω. (d) Schematic of the optimal Co-N₂ configuration with 4 epoxy groups and one O solvent species (CoN₂H₆-4O-O). The green, gray, dark blue, red and blue spheres represent the H, C, N, O, Co atom, respectively.

To further elucidate the synergy between the low-coordinated Co-N₂ configuration and C-O-C epoxide groups, density functional theory (DFT) calculations were conducted. As shown in Figure S22, a serial of Co-N₂ moieties (CoN₂H_x, $x = 4, 6, 8, 12, 14$) were constructed with the defective edge sites hydrogen-passivated for stabilizing the structure. The adsorption free energies of the *OOH intermediate (ΔG^*_{OOH}) of the 2-electron ORR process on these Co-N₂

moieties were calculated and the corresponding adsorption configurations were provided in Figure S23. **Figure 4a** shows the plot for ORR activity in terms of η as a function of ΔG^{*OOH} , showing that all considered moieties have too strong adsorption of the $^{*}OOH$ intermediate with high η for the rate-determining step ($^{*}OOH + e^{-} + H^{+} \rightarrow H_2O_2$).^[53] Among these moieties, CoN_2H_6 possesses the lowest η of 1.62 V and is thus selected as the moiety for the followed optimization by introducing epoxy groups around the Co sites. Different locations and coverages of epoxy groups near CoN_2H_6 were considered (Figure S24 and S25). When one epoxy group was introduced at the position of $1O_a$, $1O_b$, $1O_c$, $1O_d$, $1O_e$, $1O_f$, $1O_g$, $1O_h$ (Figure S24a-h), the η decreases by 0.16 V with $1O_a$ and 0.07 V with $1O_b$, while other positions that are far away from the Co site have no effects on reducing the η (Figure 4b). When increasing the coverage of epoxy groups, the η can be further reduced (Figure 4b and Figure S24i-m). Especially for the configuration with four epoxy groups nearby CoN_2H_6 (CoN_2H_6-4O), the computed η is reduced to be less than 1 V (0.97 V). Taking a step further, the solvent effects on the catalytic properties of the CoN_2H_6-4O moiety were taken into accounts by introducing the solvent species of H, O, H_2O and OH on the Co sites (Figure S26 and S27). The calculated results in Figure 4c demonstrated that the introduced H would lower the catalytic activity ($\eta = 2.10$ V), while the oxygenated species (O, H_2O and OH) could improve the activity. Among them, the OH and O solvent species are most effective in weakening the adsorption strength of $^{*}OOH$ on the Co site, leading to the significantly enhanced catalytic activity with a lower η of 0.58 and 0.42 V, respectively, in agreement with our experimental results that the Co- N_2 -C/HO catalyst is most active in alkaline media (0.1 M KOH). The schematic structural model of the optimized CoN_2H_6-4O-O moiety is displayed in Figure 4d. Besides the Co- N_2 configuration, additional calculations were performed on other Co- N_x ($x = 3$ and 4) configurations. For the Co- N_3 configuration (Figure S28a-f), the considered moieties of CoN_3H_5 , CoN_3H_5-4O and CoN_3H_5-4O-O exhibited limiting η of 1.06 V, 1.35 V and 0.54 V, respectively, while for the Co- N_4 configuration (Figure S28g-h), the considered moiety of CoN_4-4O-O exhibited a limiting

1 η of 0.64 V, further indicating that the catalytic performance is sensitive to the coordination
2 configuration and the oxygen functional groups. Therefore, these computational results jointly
3 suggest that the Co-N₂ moieties could work in synergy with the nearby epoxy groups for
4 improved catalytic activity towards the 2-electron ORR to produce H₂O₂, corroborating the
5 experimental results.

6 **3. Conclusion**

7 In summary, we demonstrated the simultaneous tuning of the coordination number and the
8 surrounding oxygen functional groups in Co-N-C catalysts by an ultra-fast heating protocol that
9 lead to the discovery of a highly active and selective catalyst for H₂O₂ electrosynthesis.
10 Compared to the typical Co-N₄-C/LO SACs, the newly developed Co-N₂-C/HO exhibited a
11 significantly enhanced performance with an early onset potential (0.801 V), a high H₂O₂
12 selectivity (91.3%), outstanding mass activity (44.4 A g⁻¹ at 0.65 V) and kinetic current density
13 (11.3 mA cm⁻² at 0.65 V). Combined experimental and theoretical analyses suggest that such
14 high performance is attributed to the unique electronic structure of Co-N₂-C/HO as a result of
15 the synergistic effects between the low-coordinated Co-N₂ configuration and the surrounding
16 C-O-C epoxide groups. This work highlights the importance of synthetic parameters and
17 procedures in affecting the atomistic structure and composition of SACs, and could motivate
18 studies on establishing the synthesis-structure-performance correlations towards the rational
19 design of SACs. Further, additional *in situ* XAS analysis can provide more information on the
20 structural changes and chemical behavior of the active sites during the H₂O₂ electrosynthesis,
21 which would contribute to the understanding of the detailed reaction mechanism and deserve
22 more research efforts in the future. On the other hand, considering the generality of the present
23 synthetic methodology, this work offers a pathway towards the exploration of catalysts with
24 unconventional structure and composition for catalyzing reactions beyond ORR, such as CO₂
25 reduction and N₂ reduction reaction.

4. Experimental Section

Synthesis of Co-N₂-C/HO: Graphene oxide (GO) was firstly prepared according to a modified Hummers' method.^[54] Amine-functionalized graphene oxide (AGO) was obtained by treating graphene oxide (GO) with NH₄OH solution. Typically, 0.288 mL of NH₄OH solution (26.5%, Sinopharm chemical) was dropwise added into 2.5 mL of GO solution (2 mg mL⁻¹) under stirring, and then stirred for another 15 min. The obtained black brown suspension was sealed in a Teflon-lined autoclave and kept at 70 °C for 5 h. After the reaction, the black suspension was washed by centrifugation repeatedly with water until the pH of the supernatant became neutral. Then, 25 µL of CoCl₂ · 6H₂O (AR, Aladdin Industrial Corporation) aqueous solution (3 mg mL⁻¹) was added dropwise into 2.5 mL of AGO suspension and stirred for 1 h. After being freeze-dried, the aerogel of Co²⁺ and AGO (Co-AGO), combined with small amounts of thermally reduced (300 °C for 1 h in Ar) graphene as initiators, were sealed in a glass tube within Ar-filled glovebox, and then microwaved (Panasonic NN-GF37JW) at 1000 W for 4 s (3 s as the induction period and 1 s as the reaction time). After cooling, the black product was collected for use. The synthesis of control samples (N-C, Co-C and LCo-N₂-C/HO) was similar to that of Co-N₂-C/HO, except without adding CoCl₂ · 6H₂O for N-C, replacing AGO with GO for Co-C, and adding 3.1 µL CoCl₂ · 6H₂O aqueous solution (3 mg mL⁻¹) into 2.5 mL of AGO suspension. To synthesize reduced Co-N₂-C/HO, Co-N₂-C/HO was reduced at 500 °C in the atmosphere of H₂/Ar (38/152 sccm) for 1.5 h with a ramping rate of 20 °C min⁻¹.

Synthesis of Co-N₄-C/LO: GO solution (2 mg mL⁻¹) was sonicated for dispersion. Then, 6.25 µL CoCl₂ · 6H₂O aqueous solution (3 mg mL⁻¹) was added dropwise into 5 mL GO solution under stirring, and then stirred for 1 h. After being freeze-dried, the Co²⁺-containing GO aerogel was loaded into a tube furnace. After continuous purging with Ar flow, the aerogel was annealed at 900 °C for 1 h with a ramping rate of 25 °C min⁻¹ under the flow of NH₃ (50 sccm) and Ar (150 sccm) to obtain Co-N₄-C/LO.

1 *Electrochemical measurements:*

2 The electrochemical measurements were conducted in a three-electrode cell equipped with a
3 rotating ring-disk electrode (RRDE, Pine Research Instrumentation, USA) setup and CHI 760E
4 electrochemical workstation. For preparing the working electrode, the catalyst ink was prepared
5 by dispersing 1 mg of catalyst into 1 mL ethanol and 20 μL Nafion (5 wt%) solution by
6 sonication for 1 h. After polishing RRDE mechanically with alumina suspension, 7.5 μL of
7 catalyst ink was drop-casted onto the disk electrode (0.196 cm^2 area) of RRDE, resulting a
8 catalyst loading of 37.5 $\mu\text{g cm}^{-2}$. Hg/HgO (1 M NaOH) electrode and graphite rod were used
9 as the reference electrode and counter electrode in 0.1 M KOH electrolyte, respectively. The
10 potentials against Hg/HgO reference electrode were converted to reversible hydrogen electrode
11 (RHE) by $E_{\text{RHE}} = E_{\text{Hg/HgO}} + 0.897$ in 0.1 M KOH based on calibration results. Electrochemical
12 measurements were conducted in an O_2 -saturated 0.1 M electrolyte. Cyclic voltammetry (CV)
13 curves were scanned from 1.2 to 0 V at a scan rate of 100 mV s^{-1} to reach a stable state. Then,
14 the LSV polarization curves were scanned from 1.0 to 0 V at a rate of 10 mV s^{-1} while keeping
15 the RRDE at a rotating speed of 1600 r.p.m. The Pt ring electrode was held at 1.2 V to quantify
16 the amount of H_2O_2 produced on the disk electrode. To subtract the contribution of background
17 current, the polarization curves were corrected by subtracting the currents measured in a N_2 -
18 saturated electrolyte. The ring collection efficiency (N) of RRDE was determined to be 0.237
19 using a typical redox system of potassium ferricyanide solution (Figure S6). The H_2O_2
20 selectivity and the number of electrons transferred can be calculated from the following
21 formulas based on the disk current (I_d) and ring current (I_r):

22
$$\text{Selectivity (\%)} = 200 \times \left(\frac{I_r}{N} \right) / \left(I_d + \frac{I_r}{N} \right)$$

23 Number of electrons transferred:

$$n = 4 \times I_d / (I_d + \frac{I_r}{N})$$

The kinetic current density (j_k) was calculated based on the measured total current density (j_m) and the diffusion-limited current density (j_l) according to Koutecký–Levich equation:

$$\frac{1}{j_m} = \frac{1}{j_l} + \frac{1}{j_k}$$

Here, the limiting current density (j_l) was derived from the steady current of the polarization curves. Chronoamperometry stability test of Co-N₂-C/HO was conducted under a constant disk electrode potential at 0.09 V in O₂-saturated 0.1 M KOH electrolyte with an RRDE rotating speed of 1600 r.p.m. After 2 h chronoamperometry test, the ring electrode was refreshed by cyclic voltammetry scanning from 0 to –0.3 V vs RHE for 40 cycles so as to remove the accumulated PtO_x species on the surface of Pt ring electrode,^[5,47] and the electrolyte was renewed with fresh electrolyte to avoid the interference of accumulated H₂O₂ to the detection of H₂O₂ oxidation current on the Pt ring electrode.

H₂O₂ concentration quantification:

To evaluate the productivity of H₂O₂, the electrochemical H₂O₂ production was conducted in an H-cell with two chambers separated by an anion-exchange membrane (Fuma FAA-PK-130). For the preparation of the working electrode, the catalyst ink was drop-casted onto the hydrophobic carbon paper (1 cm², Toray, TGP-H-060) with a catalyst loading amount of 0.1 mg cm^{–2}. The working electrode with the Hg/HgO reference electrode were placed in one chamber, and the counter electrode (graphite rod) was loaded in a separate chamber to avoid the oxidation of H₂O₂. Both chambers were filled with 25 mL of 0.1 M KOH, and the cathode chamber was bubbled with pure O₂ under stirring during electrolysis. Ethylenediamine tetraacetic acid (EDTA, 10 mM) was added into the electrolyte in the cathode chamber to inhibit

the decomposition of H₂O₂. The productivity of H₂O₂ was evaluated by chronopotentiometry at a constant current of 25 mA in the H-cell.

The concentration of the generated H₂O₂ was quantified by cerium sulfate (Ce(SO₄)₂) titration. Standard Ce(SO₄)₂ solution (0.5 mM) was prepared by dissolving Ce(SO₄)₂ salts into 0.5 M H₂SO₄ solution. The calibration curves between absorbance and H₂O₂ concentration were determined by adding different amounts of H₂O₂ solution (0.1 wt%) into the standard Ce(SO₄)₂ solution, where yellow Ce⁴⁺ cation would be reduced to colorless Ce³⁺ by H₂O₂, leading to a decline of the absorbance with the increase of H₂O₂, according to the following equation.



After electrolysis for a certain time period, 10 µL of the electrolyte in the cathode chamber was added into the standard Ce(SO₄)₂ titrant solution. By linear interpolation from the calibration curves, the concentration of H₂O₂ in the electrolyte can be calculated according to the fitted linear equation (Figure S15).

Characterization:

The compositions and structures of samples were characterized by X-ray powder diffractometer (Bruker, D8 ADVANCE), Raman spectrometer (RENISHAW inVia-reflex, 532 nm laser), X-ray photoelectron spectrometer (KRATOS AXIS SUPRA) and Fourier-transform infrared spectroscopy (Shimadzu, IR Affinity-1). Combustion elemental analysis (C, H and N) of samples were conducted on an Elementar Vario EL cube Element analyzer. The annular dark-field scanning TEM (ADF-STEM) was performed on JEOL ARM300 CF with JEOL ETA aberration correctors with beam energy 80 keV, 40 µm condenser lens aperture (32mrad), ADF detector (inner angle 47mrad) and beam current approx. 46 pA. Energy dispersive X-ray spectroscopy were measured on FEI-Titan Cubed Themis G2 300. The metal content of samples

was evaluated by inductively coupled plasma mass spectrometry (ICP-MS, Agilent 7900). The ultraviolet-visible spectroscopy of $\text{Ce}(\text{SO}_4)_2$ titrant solution was measured on Shimadzu UV-2600 spectrophotometer. Soft X-ray absorption spectra were acquired at MCD-A and MCD-B beamlines of Soochow Beamline for Energy Materials at NSRL in the total electron yield mode. Hard X-ray absorption spectra at Co K-edge were obtained at 1W1B beamline of Beijing Synchrotron Radiation Facility in fluorescence mode using a Si (111) double-crystal monochromator. A detuning of about 25% by misaligning the Si (111) crystal was performed to minimize the higher harmonics. The storage ring of BSRF was operated at 2.5 GeV with a maximum current of 250 mA in decay mode. The incident and fluorescence X-ray intensities were monitored by using standard N_2 -filled ionization chambers and Ar-filled Lytle-type detector, respectively. An energy calibration was conducted using reference bulk Co. The raw data were all background subtracted, normalized, Fourier transformed and fitted using the Demeter software.^[55]

Computational Methods:

The spin-polarized density functional theory (DFT) calculations were performed by using the Vienna ab initio Simulation Package (VASP).^[56] The generalized gradient approximation (GGA) toward Perdew-Burke-Ernzerhof (PBE) level was adopted in the projector augmented wave (PAW) potentials.^[57] The Monkhorst-Pack type of k-point sample was shifted to the gamma center to adopt for all the structures in this work. The Gaussian smearing of 0.05 eV was adopted to satisfy the self-consistence and convergence of the electron density. All the atomic positions were allowed to relax until the forces were less than $0.02 \text{ eV}/\text{\AA}$, and the electron convergence energy was set to 10^{-5} eV . The vacuum was set to 20 \AA for all the interfacial structures to avoid the interactions between its periodic images. The plane wave cutoff was set to 500 eV. The DFT-D3 scheme is adopted to correct the van der Waals interaction.^[58]

To calculate the reaction free energy profile for the electrochemical oxygen reduction reaction ($2e^-/4e^-$), the computational hydrogen electrode (CHE) model was adopted.^[59] Under standard conditions (298.15 K, 1 atm, pH=0), the free energy of H^+/e^- pair ($G(H^++e^-)$) is equivalent to that of a half of hydrogen ($1/2G(H_2)$) without applied bias (U). The reaction free energies were defined as:

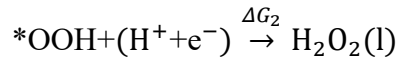
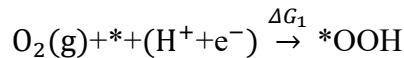
$$\Delta G = \Delta E + \Delta ZPE - T\Delta S$$

where ΔE , ΔZPE and ΔS stand for the reaction energy, differences in zero point energy and entropy, respectively. With an applied bias (U), the reaction free energies can be described as:

$$\Delta G = \Delta E + \Delta ZPE - T\Delta S - neU$$

where n is the number of electrons involved in the reaction. The 2-electron ORR can be described in the following:

2-electron ORR:



The catalytic activity of 2-electron ORR can be described by the theoretical η under the standard conditions.

For the 2-electron ORR, $\eta^{H_2O_2}$ can be given from the Gibbs free energy differences of ΔG_1 and ΔG_2 :

$$G^{H_2O_2} = \max\{\Delta G_1, \Delta G_2\}$$

$$\eta^{H_2O_2} = 0.70 \text{ V} - G^{H_2O_2}/e$$

The adsorption free energies of $*OOH$ can be taken as the descriptors for the $\eta^{H_2O_2}$ at an activity volcano diagram. The adsorption free energies are calculated as follows:

$$\Delta G_{*OOH} = G_{*OOH} - G_* - G_{OOH}$$

where G^* and G^*_{OOH} are the free energies of clean substrate and the substrate binding with $^*\text{OOH}$. G_{OOH} is the free energy of isolated gas molecules, which can be replaced by $(2G_{\text{H}_2\text{O}} - \frac{3}{2}G_{\text{H}_2})$. $G_{\text{H}_2\text{O}}$ and G_{H_2} are the energies of H_2O and H_2 in gas phase, respectively.

Supporting Information.

Supporting Information is available from the Wiley Online Library or from the author.

Acknowledgment

H.G. and Z.W. contributed equally to this work. H.F. acknowledges financial support from the National Natural Science Foundation of China (Grant No. 51902099), Hunan high-level talent gathering project (Grant No. 2019RS1021), Fundamental Research Funds for the Central Universities (Grant No. 531119200087) and the Innovative Research Groups of Hunan Province (Grant No. 2020JJ1001). S.Z. acknowledges support from the National Natural Science Foundation of China (Grant Nos. 91934302, 21878078). Z.W. acknowledges support from the China Postdoctoral Science Foundation (Grant No. 2020M683617XB). Density functional theory calculations are supported by the high-performance computing platform of Guangxi University, Guangxi Postdoctoral Innovative Talents Support Program and Guangxi Science and Technology Base and Talent Special Project. G.Y. acknowledges support from the Hunan Province Natural Science Foundation (Grant No. 2020JJ4204). J.D. acknowledges support from Youth Innovation Promotion Association CAS. We thank Diamond Light Source for access and support in use of the electron Physical Science Imaging Centre (Instrument E02, proposal number MG27260) that contributed to the results presented here. We thank the beamlines MCD-A and MCD-B (Soochow Beamline for Energy Materials) at NSRL for access and support that contributed to the results presented here.

Received: ((will be filled in by the editorial staff))

Revised: ((will be filled in by the editorial staff))

Published online: ((will be filled in by the editorial staff))

References

- [1] Z. Lu, G. Chen, S. Siahrostami, Z. Chen, K. Liu, J. Xie, L. Liao, T. Wu, D. Lin, Y. Liu, T. F. Jaramillo, J. K. Nørskov, Y. Cui, *Nat. Catal.* **2018**, *1*, 156.
- [2] H. W. Kim, M. B. Ross, N. Kornienko, L. Zhang, J. H. Guo, P. D. Yang, B. D. McCloskey, *Nat. Catal.* **2018**, *1*, 282.
- [3] K. Jiang, J. J. Zhao, H. T. Wang, *Adv. Funct. Mater.* **2020**, *30*, 2003321.
- [4] Q. Chang, P. Zhang, A. H. B. Mostaghimi, X. Zhao, S. R. Denny, J. H. Lee, H. Gao, Y. Zhang, H. L. Xin, S. Siahrostami, J. G. Chen, Z. Chen, *Nat. Commun.* **2020**, *11*, 2178.
- [5] Q. Yang, W. Xu, S. Gong, G. Zheng, Z. Tian, Y. Wen, L. Peng, L. Zhang, Z. Lu, L. Chen, *Nat. Commun.* **2020**, *11*, 5478.
- [6] E. Jung, H. Shin, W. Hooch Antink, Y.-E. Sung, T. Hyeon, *ACS Energy Lett.* **2020**, *5*, 1881.
- [7] Z. Wang, Q.-K. Li, C. Zhang, Z. Cheng, W. Chen, E. A. McHugh, R. A. Carter, B. I. Yakobson, J. M. Tour, *ACS Catal.* **2021**, *11*, 2454.
- [8] Y. Sun, I. Sinev, W. Ju, A. Bergmann, S. Dresch, S. Köhl, C. Spöri, H. Schmies, H. Wang, D. Bernsmeier, B. Paul, R. Schmack, R. Kraehnert, B. Roldan Cuenya, P. Strasser, *ACS Catal.* **2018**, *8*, 2844.
- [9] S. Yang, J. Kim, Y. J. Tak, A. Soon, H. Lee, *Angew. Chem. Int. Ed.* **2016**, *55*, 2058.
- [10] S. Siahrostami, A. Verdager-Casadevall, M. Karamad, D. Deiana, P. Malacrida, B. Wickman, M. Escudero-Escribano, E. A. Paoli, R. Frydendal, T. W. Hansen, I. Chorkendorff, I. E. L. Stephens, J. Rossmeisl, *Nat. Mater.* **2013**, *12*, 1137.
- [11] A. Verdager-Casadevall, D. Deiana, M. Karamad, S. Siahrostami, P. Malacrida, T. W. Hansen, J. Rossmeisl, I. Chorkendorff, I. E. L. Stephens, *Nano Lett.* **2014**, *14*, 1603.

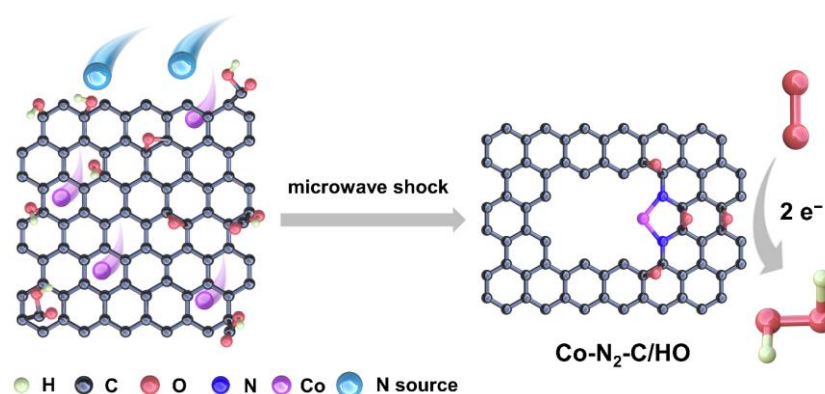
- 1 [12] H. Fei, J. Dong, D. Chen, T. Hu, X. Duan, I. Shakir, Y. Huang, X. Duan, *Chem. Soc.*
2 *Rev.* **2019**, *48*, 5207.
- 3 [13] J. Zhang, H. Yang, B. Liu, *Adv. Energy Mater.* **2020**, *11*, 2002473.
- 4 [14] C. X. Zhao, B. Q. Li, J. N. Liu, Q. Zhang, *Angew. Chem. Int. Ed.* **2021**, *60*, 4448.
- 5 [15] C. Tang, L. Chen, H. Li, L. Li, Y. Jiao, Y. Zheng, H. Xu, K. Davey, S. Z. Qiao, *J. Am.*
6 *Chem. Soc.* **2021**, *143*, 7819.
- 7 [16] R. Jiang, L. Li, T. Sheng, G. Hu, Y. Chen, L. Wang, *J. Am. Chem. Soc.* **2018**, *140*,
8 11594.
- 9 [17] H. Xu, D. Cheng, D. Cao, X. C. Zeng, *Nat. Catal.* **2018**, *1*, 339.
- 10 [18] E. Jung, H. Shin, B. H. Lee, V. Efremov, S. Lee, H. S. Lee, J. Kim, W. Hooch Antink,
11 S. Park, K. S. Lee, S. P. Cho, J. S. Yoo, Y. E. Sung, T. Hyeon, *Nat. Mater.* **2020**, *19*,
12 436.
- 13 [19] Q. Zhang, X. Tan, N. M. Bedford, Z. Han, L. Thomsen, S. Smith, R. Amal, X. Lu,
14 *Nat. Commun.* **2020**, *11*, 4181.
- 15 [20] W. I. Choi, B. C. Wood, E. Schwegler, T. Ogitsu, *Adv. Energy Mater.* **2015**, *5*,
16 1501423.
- 17 [21] C. H. Choi, H.-K. Lim, M. W. Chung, G. Chon, N. Ranjbar Sahraie, A. Altin, M.-T.
18 Sougrati, L. Stievano, H. S. Oh, E. S. Park, F. Luo, P. Strasser, G. Dražić, K. J. J.
19 Mayrhofer, H. Kim, F. Jaouen, *Energy Environ. Sci.* **2018**, *11*, 3176.
- 20 [22] B. Q. Li, C. X. Zhao, J. N. Liu, Q. Zhang, *Adv. Mater.* **2019**, *31*, 1808173.
- 21 [23] X. X. Wang, M. T. Swihart, G. Wu, *Nat. Catal.* **2019**, *2*, 578.
- 22 [24] Q. Lai, L. Zheng, Y. Liang, J. He, J. Zhao, J. Chen, *ACS Catal.* **2017**, *7*, 1655.
- 23 [25] C. Yan, H. Li, Y. Ye, H. Wu, F. Cai, R. Si, J. Xiao, S. Miao, S. Xie, F. Yang, Y. Li, G.
24 Wang, X. Bao, *Energy Environ. Sci.* **2018**, *11*, 1204.
- 25 [26] X. Rong, H. J. Wang, X. L. Lu, R. Si, T. B. Lu, *Angew. Chem., Int. Ed.* **2020**, *59*,
26 1961.

- 1 [27] Y. J. Sa, H. Jung, D. Shin, H. Y. Jeong, S. Ringe, H. Kim, Y. J. Hwang, S. H. Joo,
2 *ACS Catal.* **2020**, *10*, 10920.
- 3 [28] Y. N. Gong, L. Jiao, Y. Qian, C. Y. Pan, L. Zheng, X. Cai, B. Liu, S. H. Yu, H. L.
4 Jiang, *Angew. Chem., Int. Ed.* **2020**, *59*, 2705.
- 5 [29] X. Wang, Z. Chen, X. Zhao, T. Yao, W. Chen, R. You, C. Zhao, G. Wu, J. Wang, W.
6 Huang, J. Yang, X. Hong, S. Wei, Y. Wu, Y. Li, *Angew. Chem.* **2018**, *57*, 1944.
- 7 [30] D. X. Luong, K. V. Bets, W. A. Algozeeb, M. G. Stanford, C. Kittrell, W. Chen, R. V.
8 Salvatierra, M. Ren, E. A. Mchugh, P. A. Advincula, Z. Wang, M. Bhatt, H. Guo, V.
9 Mancevski, R. Shahsavari, B. I. Yakobson, J. M. Tour, *Nature* **2020**, *577*, 647.
- 10 [31] Y. Yao, Z. Huang, P. Xie, L. Wu, L. Ma, T. Li, Z. Pang, M. Jiao, Z. Liang, J. Gao, Y.
11 He, D. J. Kline, M. R. Zachariah, C. Wang, J. Lu, T. Wu, T. Li, C. Wang, R.
12 Shahbazian-Yassar, L. Hu, *Nat. Nanotechnol.* **2019**, *14*, 851.
- 13 [32] H. Fei, J. Dong, C. Wan, Z. Zhao, X. Xu, Z. Lin, Y. Wang, H. Liu, K. Zang, J. Luo, S.
14 Zhao, W. Hu, W. Yan, I. Shakir, Y. Huang, X. Duan, *Adv. Mater.* **2018**, *30*, e1802146.
- 15 [33] J. Y. Damien Voiry, 1† Jacob Kupferberg, 1 Raymond Fullon, 1 Calvin Lee, 1 Hu
16 Young Jeong, 2 Hyeon Suk Shin, 3 Manish Chhowalla, *Science* **2016**, *353*, 1413.
- 17 [34] S. Xu, G. Zhong, C. Chen, M. Zhou, D. J. Kline, R. J. Jacob, H. Xie, S. He, Z. Huang,
18 J. Dai, A. H. Brozena, R. Shahbazian-Yassar, M. R. Zachariah, S. M. Anlage, L. Hu,
19 *Matter* **2019**, *1*, 759.
- 20 [35] S. C. Perry, D. Pangotra, L. Vieira, L.-I. Csepei, V. Sieber, L. Wang, C. Ponce De
21 León, F. C. Walsh, *Nat. Rev. Chem.* **2019**, *3*, 442.
- 22 [36] Y. Yao, Z. Huang, P. Xie, S. D. Lacey, R. J. Jacob, H. Xie, F. Chen, A. Nie, T. Pu, M.
23 Rehwoldt, D. Yu, M. R. Zachariah, C. Wang, R. Shahbazian-Yassar, J. Li, L. Hu,
24 *Science* **2018**, *359*, 1489.

- 1 [37] Y. Yao, Z. Liu, P. Xie, Z. Huang, T. Li, D. Morris, Z. Finfrock, J. Zhou, M. Jiao, J.
2 Gao, Y. Mao, J. J. Miao, P. Zhang, R. Shahbazian-Yassar, C. Wang, G. Wang, L. Hu,
3 *Sci. Adv.* **2020**, *6*, eaaz0510.
- 4 [38] W. Chen, Z. Wang, K. V. Bets, D. X. Luong, M. Ren, M. G. Stanford, E. A. Mchugh,
5 W. A. Algozeeb, H. Guo, G. Gao, B. Deng, J. Chen, J. T. Li, W. T. Carsten, B. I.
6 Yakobson, J. M. Tour, *ACS Nano* **2021**, *15*, 1282.
- 7 [39] D. Xia, X. Yang, L. Xie, Y. Wei, W. Jiang, M. Dou, X. Li, J. Li, L. Gan, F. Kang,
8 *Adv. Funct. Mater.* **2019**, *29*, 1906174.
- 9 [40] K. Jiang, S. Siahrostami, T. T. Zheng, Y. F. Hu, S. Hwang, E. Stavitski, Y. D. Peng, J.
10 Dynes, M. Gangisetty, D. Su, K. Attenkofer, H. T. Wang, *Energy Environ. Sci.* **2018**,
11 *11*, 893.
- 12 [41] C. H. van Oversteeg, H. Q. Doan, F. M. de Groot, T. Cuk, *Chem. Soc. Rev.* **2017**, *46*,
13 102.
- 14 [42] E. Brillas, I. Sirés, M. A. Oturan, *Chem. Rev.* **2009**, *109*, 6570.
- 15 [43] Z. Zheng, Y. H. Ng, D.-W. Wang, R. Amal, *Adv. Mater.* **2016**, *28*, 9949.
- 16 [44] Y. Wang, R. Shi, L. Shang, G. I. N. Waterhouse, J. Zhao, Q. Zhang, L. Gu, T. Zhang,
17 *Angew. Chem., Int. Ed.* **2020**, *59*, 2.
- 18 [45] L. Li, C. Tang, Y. Zheng, B. Xia, X. Zhou, H. Xu, S. Z. Qiao, *Adv. Energy Mater.*
19 **2020**, *10*, 2000789.
- 20 [46] C. Tang, Y. Jiao, B. Shi, J. N. Liu, Z. Xie, X. Chen, Q. Zhang, S. Z. Qiao, *Angew.*
21 *Chem., Int. Ed.* **2020**, *59*, 9171.
- 22 [47] K. Jiang, S. Back, A. J. Akey, C. Xia, Y. Hu, W. Liang, D. Schaak, E. Stavitski, J. K.
23 Norskov, S. Siahrostami, H. Wang, *Nat. Commun.* **2019**, *10*, 3997.
- 24 [48] A. Verdager-Casadevall, P. Hernandez-Fernandez, I. E. L. Stephens, I. Chorkendorff,
25 S. Dahl, *J. Power Sources* **2012**, *220*, 205.
- 26 [49] J. S. Jirkovský, M. Halasa, D. J. Schiffrin, *Phys. Chem. Chem. Phys.* **2010**, *12*, 8042.

- 1 [50] Y. Sun, L. Silvioli, N. R. Sahraie, W. Ju, J. Li, A. Zitolo, S. Li, A. Bagger, L.
2 Arnarson, X. Wang, T. Moeller, D. Bernsmeier, J. Rossmeisl, F. Jaouen, P. Strasser, *J.*
3 *Am. Chem. Soc.* **2019**, *141*, 12372.
- 4 [51] C. H. Choi, W. S. Choi, O. Kasian, A. K. Mechler, M. T. Sougrati, S. Brüller, K.
5 Strickland, Q. Jia, S. Mukerjee, K. J. J. Mayrhofer, F. Jaouen, *Angew. Chem., Int. Ed.*
6 **2017**, *56*, 8809.
- 7 [52] D. Zhao, Z. Zhuang, X. Cao, C. Zhang, Q. Peng, C. Chen, Y. Li, *Chem. Soc. Rev.*
8 **2020**, *49*, 2215.
- 9 [53] A. Kulkarni, S. Siahrostami, A. Patel, J. K. Nørskov, *Chem. Rev.* **2018**, *118*, 2302.
- 10 [54] W. S. Hummers, R. E. Offeman, *J. Am. Chem. Soc.* **1958**, *80*, 1339.
- 11 [55] B. Ravel, M. Newville, *J. Synchrotron Radiat.* **2005**, *12*, 537.
- 12 [56] G. Kresse, J. Furthmüller, *Phys. Rev. B* **1996**, *54*, 11169.
- 13 [57] J. P. Perdew, K. Burke, M. Ernzerhof, *Phys. Rev. Lett.* **1996**, *77*, 3865.
- 14 [58] S. Ehrlich, J. Moellmann, W. Reckien, T. Bredow, S. Grimme, *ChemPhysChem* **2011**,
15 *12*, 3414.
- 16 [59] J. K. Nørskov, J. Rossmeisl, A. Logadottir, L. Lindqvist, J. R. Kitchin, T. Bligaard, H.
17 Jónsson, *J. Phys. Chem. B* **2004**, *108*, 17886.
- 18

Table of Contents:



A low-coordinated Co-N₂-C single-atom catalyst containing abundant C-O-C epoxide groups is developed *via* a transient microwave thermal shock with merits of optimized electronic structure and exceptional performance for H₂O₂ production.